Contributions of Jupiter's Deep-Reaching Surface Winds to Magnetic Field Structure and Secular Variation

J. Wicht[1] and U. R. Christensen[1]

[1]Max Planck Institute for Solar System Research, Göttingen, Germany

Abstract NASA's Juno mission delivered gravity data of exceptional quality. They indicate that the zonal winds, which rule the dynamics of Jupiter's cloud deck, must slow down significantly beyond a depth of about 3,000 km. Since the underlying inversion is highly non-unique additional constraints on the flow properties at depth are required. These could potentially be provided by the magnetic field and its Secular Variation (SV) over time. However, the role of these zonal winds in Jupiter's magnetic field dynamics is little understood. Here we use numerical simulations to explore the impact of the zonal winds on the dynamo field produced at depth. We find that the main effect is an attenuation of the non-axisymmetric field, which can be quantified by a modified magnetic Reynolds number Rm that combines flow amplitude and electrical conductivity profile. Values below Rm = 3 are required to retain a pronounced non-axisymmetric feature like the Great Blue Spot (GBS), which seems characteristic for Jupiter's magnetic field. This allows for winds reaching as deep as 3,400 km. A SV pattern similar to the observation can only be found in some of our models. Its amplitude reflects the degree of cancellation between advection and diffusion rather than the zonal wind velocity at any depth. It is therefore not straightforward to make inferences on the deep structure of cloud-level winds based on Jupiter's SV.

Plain Language Summary The dynamics in Jupiter's cloud layer is dominated by eastward and westward directed wind jets that circumvent the planet and reach velocities of up to 150 m per second. For the first time, NASA's Juno mission could measure the tiny gravity changes caused by these winds. The data show that the winds reach down to a depth of about 3,000 km, roughly 4% of Jupiter's radius. However, the interpretation is difficult and several alternative wind profiles have been suggested. In this paper we use numerical simulations to explore how these winds would affect Jupiter's magnetic field, which has also been measured with high precision by Juno. The field shows a strong inward-directed local patch just south of the equator, called the GBS. The impact of the winds on the magnetic field rapidly increases with depth because of the increase in the electrical conductivity. Our simulations show that winds reaching deeper than about 3,400 km would practically wipe out the GBS. This confirms that they have to remain shallower. Juno also observed an east-ward drift of the GBS. While some of our simulations also show an east-ward drift it is typically much too slow.

1. Introduction

One of the primary objectives of the NASA's Juno mission was to determine the depth of the zonal winds observed in Jupiter's cloud deck. The highly precise gravity measurements were able to constrain that the winds reach down to roughly 3,000 km (Kaspi et al., 2018). However, deducing flow properties from their gravity impact is highly non-unique and several competing models have been suggested (Dietrich et al., 2021; Galanti & Kaspi, 2021; Kaspi et al., 2018; Kong et al., 2018; Kulowski et al., 2021). Any additional information on the wind properties at depth remains very valuable.

The detailed observations of the Secular Variation (SV) of Earth's magnetic field have been used since decades to deduce the flows at the top of Earth's core (see for example, Holme, 2015). The low electrical conductivity and vanishing flow velocity in Earth's mantle guarantees that its contribution to the magnetic field is negligible. We can therefore attribute the observed variations to the core dynamics. And since magnetic induction clearly dominates diffusion, these variations can be interpreted as advective modifications of the magnetic field in the so-called frozen-flux approximation. The ratio of induction to diffusion is typically quantified by the magnetic Reynolds number,
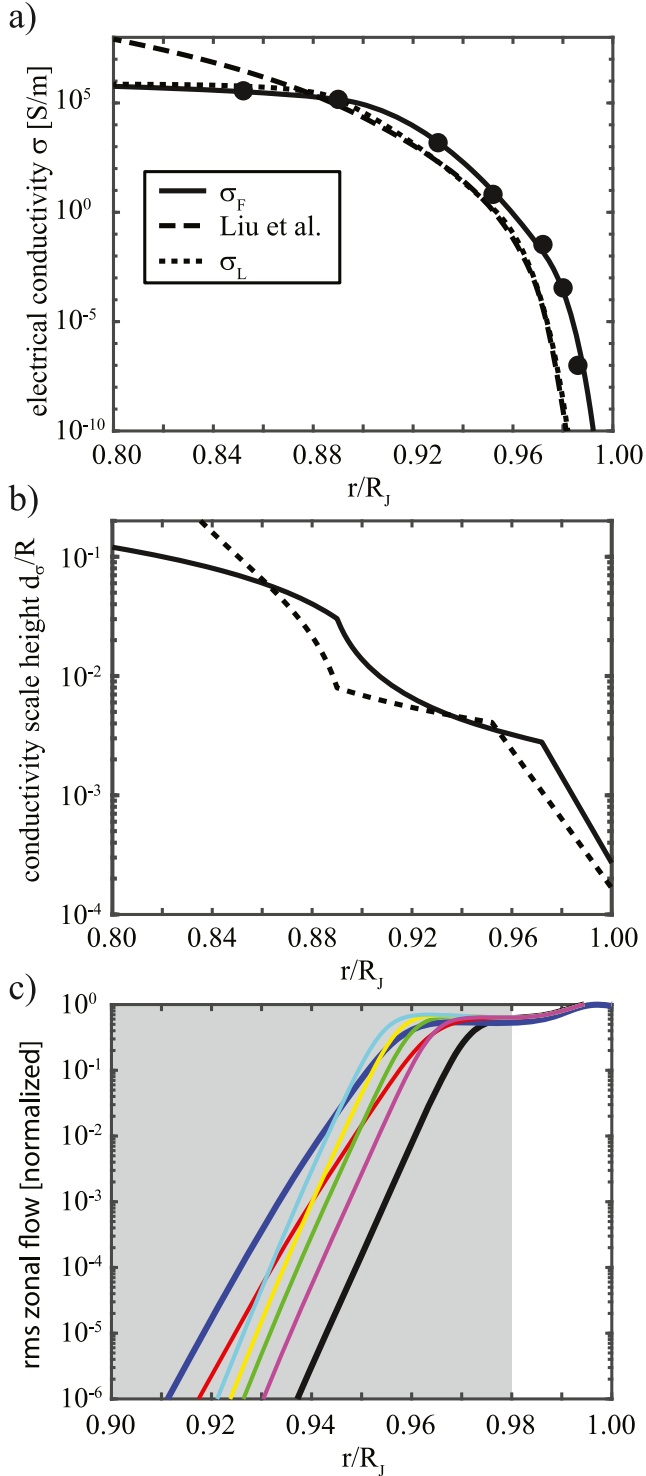
Figure 1. Electrical conductivity models (a), respective diffusivity scale heights (b), and rms zonal flow velocities for the seven zonal flow models (c). The electrical conductivity models σ_F and σ_L refer to the models by French et al. (2012) and Liu et al. (2008) respectively. The parameters of the zonal flows models U1 (black), U2 (magenta), U3 (green), U4 (red), U5 (yellow), U6 (blue), and U7 (cyan) are given in Table 1.

$$\mathrm{Rm} = \frac{Ud}{\lambda}, \tag{1}$$

where U is a typical flow velocity, d a typical length scale, and $\lambda = 1/(\mu\sigma)$ the magnetic diffusivity with μ the magnetic permeability and σ the electrical conductivity. Since Rm is about 2000 for Earth's core, the frozen-flux approximation is clearly warranted for time scales of decades to centuries. Inverting the SV for the unknown flow at the top of Earth's core still requires additional assumptions. We refer to Schwaiger et al. (2023) for a recent discussion.

In Jupiter, the conductivity increases rapidly with depth due to ionization. At about 10% in radius, hydrogen becomes metallic and the conductivity grows much less steeply over the remaining interior (French et al., 2012; Liu et al., 2008). If the downward-projected zonal winds retain a sufficient amplitude at a depth where the conductivity becomes sufficiently high they could indeed leave a magnetic signature that may carry information on the deeper flow properties.

Moore et al. (2019) analyzed Jupiter magnetic field data that have been collected over a period of 40 years by various spacecrafts. They report that the SV can be explained by an eastward advection of the Great Blue Spot (GBS), a prominent feature of Jupiter's magnetic field just south of the equator (Connerney et al., 2018, 2022) (see Figure 6). Moore et al. (2019) assume that the latitudinal wind structure observed at cloud level remains invariant along cylinders aligned with the rotation axis, which is typical for the dynamics in fast rotating systems. According to Moore et al. (2019), the SV then suggest maximum zonal flow amplitudes in the range of a few *cm/s* acting at depths between 0.93 R_J and 0.95 R_J, where R_J is Jupiter's mean radius. This would correspond to local magnetic Reynolds numbers,

$$\mathrm{Rm}(r) = \frac{Ud_\lambda}{\lambda}, \tag{2}$$

with values between 0.1 and 10, where U, λ, and the magnetic diffusivity scale height

$$d_\lambda = \frac{\lambda}{\partial\lambda/\partial r} \tag{3}$$

reflect typical values at a given radius. For such low Rm values, we expect a significant contribution of diffusion and it thus seems questionable to directly translate the SV to flow velocities.

Motivated by the results from Moore et al. (2019), Galanti and Kaspi (2021) modified earlier inversions of Juno gravity data (Kaspi et al., 2018; Kong et al., 2018) to yield a much steeper decay of the flow amplitude with depth. The revised zonal flows reach to a depth of only about 2,300 km but still explain the gravity data when allowing for a small modifications of the latitudinal wind structure compared to what is observed at the cloud deck. Recent analyses based on a high-degree gravity model strengthened the case for an alignment of the winds with the rotation axis (Kaspi et al., 2023) and for a close match of the deeper flow with the observed surface winds (Cao et al., 2023).

The longer mission duration of the Juno spacecraft recently allowed to deduce the SV based on the mission data alone. Connerney et al. (2022) and Bloxham

Table 1
Overview of the Explored Flow Models: Column 2 List the Model Name and Column 3 the Color Signifying the Model in Several Figures

#	Name	Color	H[km]	δ[km]	D[km]
1	U1	black	2,000	350	2,300
2	U2	magenta	2,500	350	2,800
3	U3	red	2,500	500	3,000
4	U4	green	2,800	350	3,100
5	U5	yellow	3,000	350	3,300
6	U6	blue	3,000	500	3,400
7	U7	cyan	3,200	350	3,500

Note. Columns 4 and 5 provide the parameters of the radial profile Q and column 6 lists the depth D where the rms flow amplitude has decreased to 10% of its surface value.

et al. ([2022](#)) show that this SV is clearly dominated by an eastward drift of the GBS with a velocity of about 0.5 cm/s (or somewhat larger). A straight-forward way to explain this is a small correction of Jupiter's rotation rate by 0.1°/yr, which amounts to only about 1 part in 10^6 of System III (1965) rotation based on tracking the magnetic field related radio emission. Bloxham et al. ([2022](#)) also show that a somewhat better fit to the data can be obtained by a model where the field is advected by zonal winds with large-scale latitudinal variations that deviate from solid-body rotation. They speculate that these flows are not related to the downward continued surface winds but rather reflect the dynamics of the deeper dynamo process.

Cao and Stevenson ([2017](#)) and Wicht et al. ([2019a](#)) estimate the changes in the radial (poloidal) magnetic field that would be caused by the action of the zonal winds, focusing on the quasi-steady state where the modification of the field produced by the deeper dynamo is balanced by magnetic diffusion. Such a state will be approximated when the time $\mathcal{T}_d$ required to reach it is shorter than the typical variation time $\mathcal{T}_b$ of the deep dynamo field. We will further discuss these time scales in Section [2.2](#). Jupiter-like dynamo simulations suggest that the zonal wind action rather than the α-effect has the strongest impact on the radial magnetic field (Wicht, Gastine, & Duarte, [2019](#)). This lead Wicht et al. ([2019a](#)) to propose the simpler estimate of the induced poloidal field

$$\mathrm{B} \approx \mathrm{Rm}\,(d_\lambda/d_\phi)\,\mathrm{B}_b, \tag{4}$$

where d_ϕ is the typical azimuthal length scale of the background field $\mathbf{B}_b$. Wicht et al. ([2019a](#)) argue that this linear estimate only makes sense in the very outer region of Jupiter where $\mathrm{Rm}\,(d_\lambda/d_\phi) < 1$ so that the locally induced field would remain smaller than the background field.

Jupiter's magnetic field structure and secular variation is certainly ruled by the deep dynamo process, but the deep-reaching surface winds may also play a role. The fact that we have some idea of the latitudinal wind structure should help to identify their contribution. Comparing model predictions of wind-induced field changes with the observed structure and secular variation allows to tighten the constraints on the depth-dependence of the winds. However, the strong impact of diffusion and the depth dependence of the flow amplitude and of the electrical conductivity complicates the interpretation.

Ideally, one would explore the impact of zonal flows in a 3d numerical simulation of Jupiter's interior where magnetic field and zonal flows are produced self-consistently by the convection driven dynamics. Attempts in this direction show some interesting results (Gastine & Wicht, [2021](#); Yadav et al., [2022](#)) but also fail to reproduce some key properties that are important for the issues explore here. The zonal jets are less numerous and much slower in comparison to other flow components than on Jupiter. Furthermore, pronounced local magnetic field structures like the GBS are missing. We therefore chose a simpler approach where the zonal winds and the deep dynamo field are prescribed. Modeling only the outer 8%–10% of Jupiter's radius, we numerically explore the impact of different zonal wind models for two different electrical conductivity profiles. Radial flows are neglected altogether. In addition to predicting the field modifications we specifically address the question what the SV could tell us about the downward-continued zonal winds at depth.

2. Model Setup

2.1. Model Equations

Being interested in the observable poloidal field, we solve the radial component of the induction equation:
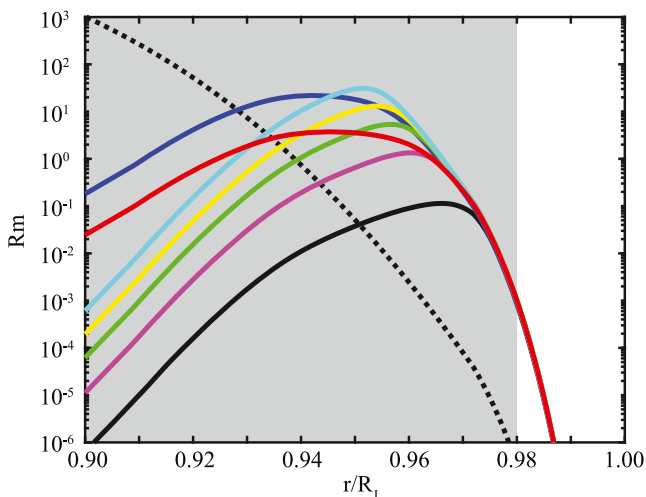
Figure 2. Magnetic Reynolds numbers for conductivity model σ_F and our seven color coded flow models (see Figure [1c](#) and Table [1](#)). The black dotted line illustrates the case when assuming a constant velocity of 1 cm/s.

Table 2
Overview of the Explored Models

#	name	Backg.	Cond.	r_i/R_J	r_o/R_J	Rm_{max}	Δb	$\partial B_r/\partial t$	Time [yr]
1	U1SF	I	σ_F	0.92	0.98	0.11	2.2×10^{-4}	-4.9×10^{-5}	50
2	U2SF	I	σ_F	0.90	0.98	1.3	2.6×10^{-2}	-3.8×10^{-3}	50
3	U3SF	I	σ_F	0.90	0.98	3.7	7.7×10^{-2}	-1.4×10^{-2}	50
4	U4SF	I	σ_F	0.90	0.98	5.4	1.2×10^{-1}	-1.3×10^{-2}	50
5	U5SF	I	σ_F	0.90	0.98	13	2.6×10^{-1}	-1.7×10^{-2}	100
6	U6SF	I	σ_F	0.90	0.98	22	4.9×10^{-1}	-2.6×10^{-2}	100
7	U6SF_JRM33	I	σ_F	0.90	0.98	22	4.4×10^{-1}	-5.8×10^{-2}	50
8	U6SF_SBR	I	σ_F	0.90	0.98	26	8.2×10^{-1}	$-4. \times 10^{-2}$	50
9	U1SL	I	σ_L	0.92	0.97	0.01	0.0	-1.6×10^{-6}	40
10	U2SL	I	σ_L	0.90	0.97	0.17	5.4×10^{-4}	-8.6×10^{-5}	50
11	U4SL	I	σ_L	0.90	0.97	0.86	1.2×10^{-2}	-1.6×10^{-3}	50
12	U5SL	I	σ_L	0.90	0.97	2.3	4.2×10^{-2}	-2.6×10^{-2}	50
13	U6SL	I	σ_L	0.90	0.97	3.1	8.6×10^{-2}	-6.1×10^{-3}	100
14	U6SL_JRM33	I	σ_L	0.90	0.97	3.1	7.8×10^{-2}	-1.3×10^{-2}	50
15	U7SL	I	σ_L	0.90	0.97	5.7	1.0×10^{-1}	-9.3×10^{-3}	50
16	U1SFe	E	σ_F	0.92	0.98	0.11	3.0×10^{-4}	1.5×10^{-1}	150
17	U3SFe	E	σ_F	0.92	0.98	3.7	9.8×10^{-2}	1.5×10^{-1}	150
18	U5SFe	E	σ_F	0.92	0.98	13	2.6×10^{-1}	1.5×10^{-1}	150
19	U6SFe	E	σ_F	0.92	0.98	22	4.5×10^{-1}	7.1×10^{-2}	175
20	U6SLe	E	σ_L	0.92	0.97	3.1	5.7×10^{-2}	-4.8×10^{-6}	130

Note. Column 2 list the model name: the two first characters signify the flow model while the next two characters indicate the conductivity model. Column 3 indicates the initial background field model, either instant (I) or emerging (E), and column 4 lists the conductivity model. Columns 5 and 6 list the inner and outer radius in units of R_J. Column 7 gives the maximum Rm. Column 8 provides the relative attenuation Δb of the rms non-axisymmetric field B_r' at the end of the time integration and column 9 gives the relative change in rms radial field (units $B_{br}/100$ yr) at the end of the integration. Finally, column 10 gives the total integration time in years. Model 8 uses the simple flow structure without latitudinal shear. Models 7 and 14 use JRM33 rather then JRM09 as a background field.

$$\frac{\partial}{\partial t} B_r = -\mathbf{U} \cdot \nabla \, B_r \, + \lambda \, \nabla^2 \, B_r. \tag{5}$$

We focus on the effects of zonal flows $\mathbf{U} = U(r,\theta) \, \hat{\phi}$, which clearly dominate the cloud-deck dynamics. The radial component of the induction equation then simplifies to

$$\frac{\partial}{\partial t} B_r = -\frac{U}{r \sin(\theta)} \, \frac{\partial}{\partial \phi} B_r \, + \lambda \, \nabla^2 \, B_r, \tag{6}$$

where θ is the colatitude and ϕ the longitude. This process would not create any field from scratch but we assume that a deeper dynamo process produces an internal background field B_b that is then modified by the zonal flows.

The background field is imposed by a lower magnetic boundary condition. The choice of the initial state is problematic and somewhat arbitrary. We follow two different approaches that may represent a kind of end-members. In the instant background field approach we impose the radial component of the field, fixed in time, at the lower boundary,

$$B_r(r_i) = B_{br}(r_i), \tag{7}$$
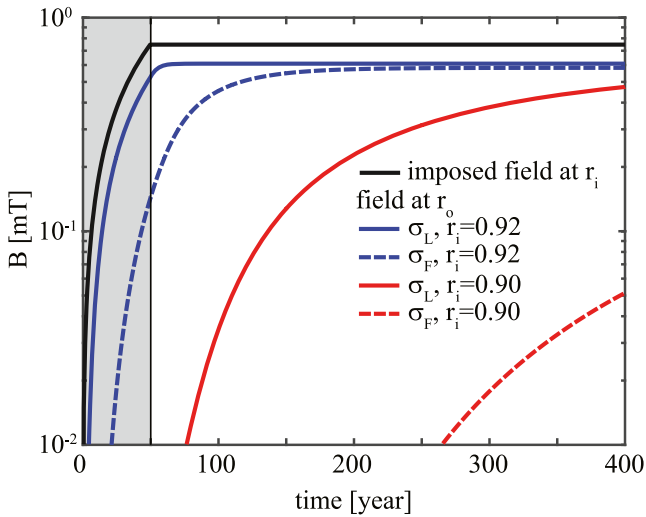
Figure 3. Evolution of the rms magnetic field for the emerging initial field simulations where the field is imposed at the bottom (black), linearly growing over 50 years, and diffuses to the outer boundary of the simulations, $r_o = 0.98\,R_J$ for σ_F and $r_o = 0.97\,R_J$ for σ_L. Colored lines show the evolution of the rms field at the outer boundary for the two conductivity models σ_F (dashed) and σ_L (solid) and lower boundaries at $r_i = 0.92\,R_J$ (blue) and $r_i = 0.90\,R_J$ (red).

and upward continue it as a potential field throughout the simulation shell. This potential field serves as the initial condition. The rationale behind imposing a fixed radial field at the lower boundary is the idea that the increasing conductivity would tend to prevent the locally produced field from penetrating deeper.

Obviously, the internal field itself will also change with time. For a simple exploration of related issues we impose an emerging radial internal field at the lower boundary that grows linearly for $t \leq t_e$,

$$B_r(r_i) = (t/t_e)\, B_{br}(r_i), \qquad (8)$$

and then remains constant for $t > t_e$. The field is initially zero and then diffuses upward toward the outer boundary. This is certainly an unrealistic scenario for Jupiter. However, since we explore a linear system it nevertheless serves to illustrates the effects on individual emerging or changing magnetic field features. Because of the linearity, an emerging structure such as a growing GBS can be thought of as being superimposed on a background field without interaction.

Details of the numerical methods used to integrate the system in time are given in the Appendix A1. We have developed the Matlab package SVzon to perform the simulations and to analyze and plot the results. SVzon is publicly available along with the simulation results at the repository EDMOND (Wicht, 2023).

2.2. Choosing Jupiter Models

We have to chose a background field, an electrical conductivity model and a zonal flow model. The Jupiter field model JRM09 (Connerney et al., 2018) up to degree and order 10 serves as the background field. Tests with the updated model JRM33 (Connerney et al., 2022) up to degree and order 13 yield practically identical results, as we demonstrate below.

Figure 1a compares the two electrical conductivity models explored here. The model by French et al. (2012), denoted σ_F (solid line), is based on ab-initio calculations, while the model by Liu et al. (2008) has been fitted to two data points from shock experiments. Our respective parametrization σ_L (dotted) differs from Liu et al. (2008) (dashed) below about 0.92 R_J to capture the transition to the metallic hydrogen region at around 0.9 R_J. The electrical conductivity scale heights, d_λ, are shown in Figure 1b.

Our zonal flow models match the observed surface zonal flows U_0 by Porco et al. (2003). These are downward continued by assuming cylindrical geometry, that is, the latitudinal structure only depends on the distance $s = r\sin\theta$ to the rotation axis. Because this procedure introduces discontinuities at the equator, we smooth the flow model in colatitude and radius. The smoothing also gets rid of some small scale variations in the surface flow that may only represent seasonal weather features. Details on the smoothing procedure can be found in the Appendix A2. The cylindrical geometry is suggested by theoretical consideration, laboratory experiments, and numerical simulations (see Wicht & Gastine, 2020 for a brief overview).

An additional radial profile $Q(r)$ describes the decay of the wind velocity with depth:

$$U(r,\theta) = Q(r)\, U_0(s). \qquad (9)$$

The gravity data measured by the Juno spacecraft have been used to constrain $Q(r)$, in particular the odd gravity harmonics up to degree $\ell = 11$ which cannot be caused by the rotational deformation of Jupiter (Kaspi et al., 2018; Kong et al., 2018). Our model U1 is very close to the rather shallow flow suggested by Galanti and Kaspi (2021) in response to the magnetic constraints (Moore et al., 2019). The black line in Figure 1c shows the respective rms flow speed. In order to still explain the gravity observations, Galanti and Kaspi (2021) slightly modify the
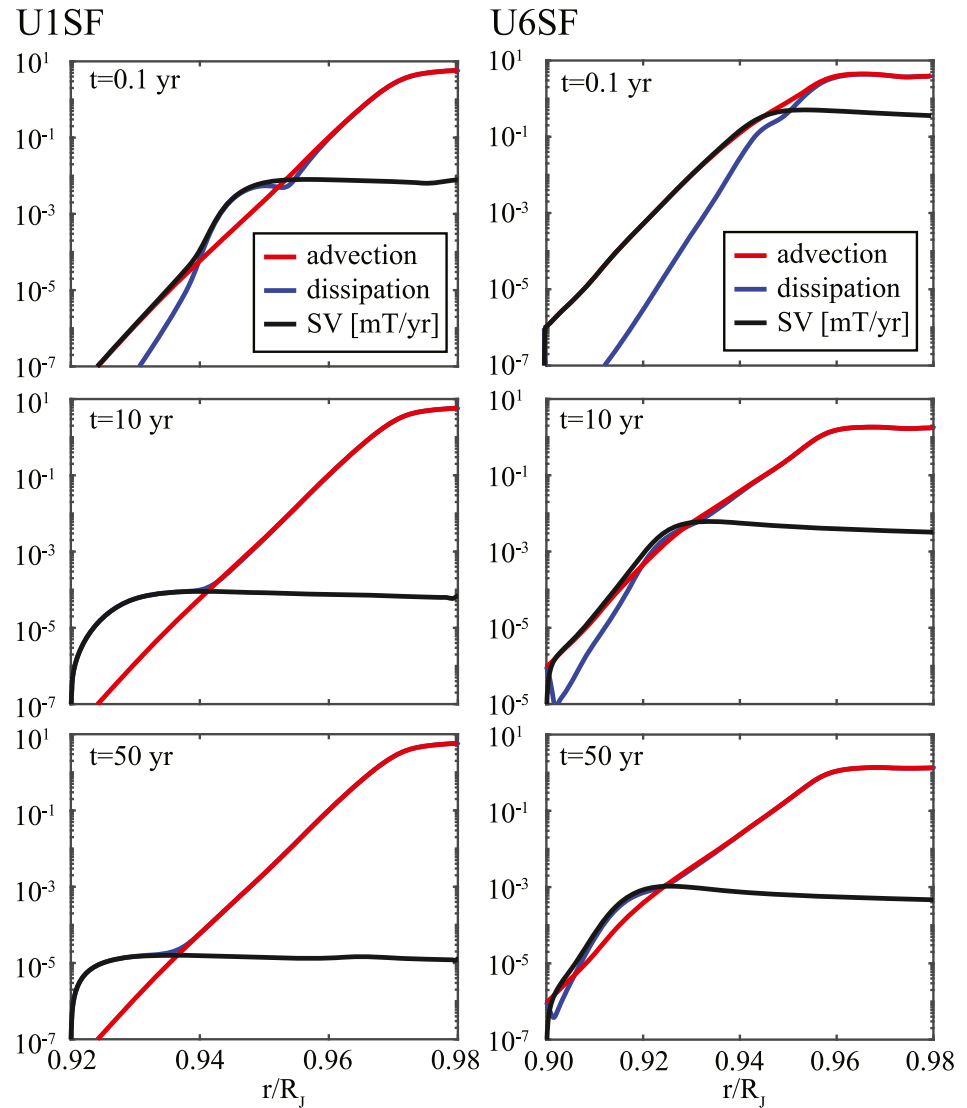
Figure 4. Radial profiles of the rms contributions to the radial induction equation for flow U1 (left) and flow U6 (right) at three different times. Conductivity model σ_F has been used.

latitudinal wind structure. Since the modifications have not been specified we use the unmodified version. Tests have shown that the details of the flow structure do not matter for our analysis.

Dietrich et al. (2021) present an alternative model where the winds extend to somewhat greater depth but still explain the gravity observations. This forms our model U6. Motivated by the flow structure in numerical dynamo simulations, Dietrich et al. (2021) neglected any equatorially antisymmetric zonal flow contributions between +21° and −21° latitude. We adopt this model as U6 but found that this latitude cut-off does not affect the results presented here.

The depth profiles of all models are defined by the hyperbolic tangent function

$$Q(r) = \left[\tanh\left(\frac{r - R + H}{\delta}\right) + 1\right] \Bigg/ \left[\tanh\left(\frac{H}{\delta}\right) + 1\right]. \tag{10}$$

Altogether, seven different flow models are explored whose parameters are listed in Table 1; Figure 1c shows the radius dependence of the rms flow amplitudes $U(r)$. The drop in rms flow speed around 0.99 R results from the fact that this is the depth where the fast equatorial jet stops contributing.

a)

b)
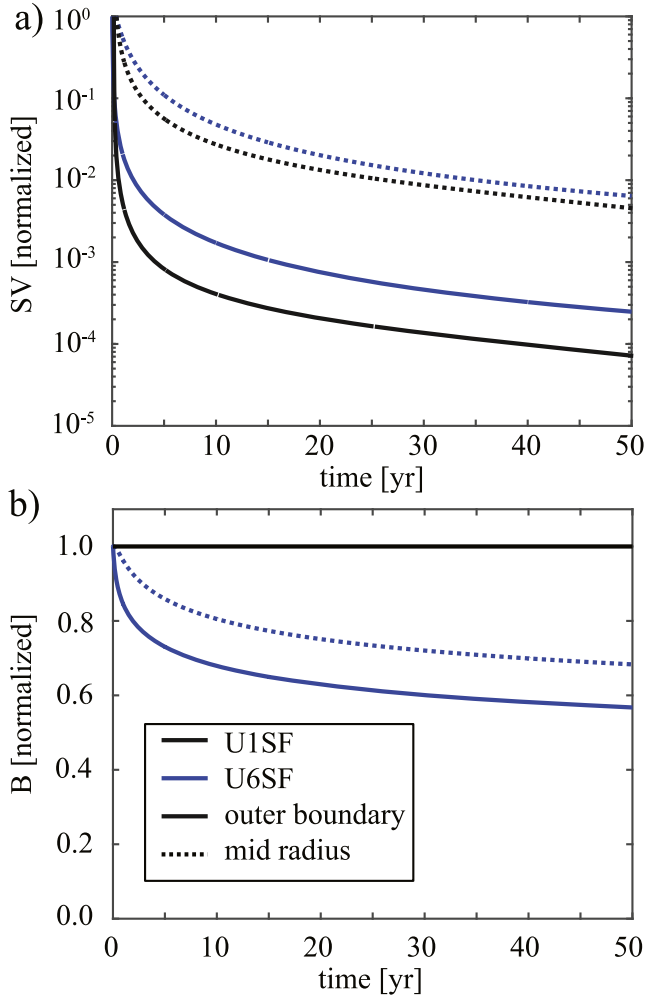
Figure 5. Rms values of the SV (a) and radial field (b) at the outer boundary r_o (solid) and at mid shell $(r_o + r_i)/2$ (dotted). The values have been normalized with the respective first stored values. Black (blue) lines show results for flow model U1 (U6) and conductivity model σ_F. The dotted black line for the mid-shell rms field (b) for flow U1 is covered by the respective solid black line for the outer-boundary value.

We define the depth D of a flow model as the depth where the rms amplitude has reached 10% of its surface value. U1 is the most shallow flow model explored here with $D = 2,300$ km. U6 is the second deepest-reaching with $D = 3,400$ km. The deepest model is U7 with $D = 3,500$ km.

Figure 2 shows profiles of the local magnetic Reynolds number Rm, Equation 2, that result from combining the rms flow profiles $U(r)$ with the conductivity model σ_F. Values for σ_L are about an order of magnitude smaller. Because of the rapidly decreasing conductivity, Rm becomes so low in the outer few percent in radius that any magnetic effects can be neglected. We therefore restrict our calculation to $r \leq 0.98$ R for σ_F and $r \leq 0.97$ R for σ_L. Table 2 lists the parameters for all the simulations we performed, including the maximum local magnetic Reynolds number Rm_{max} reached in each model (column 7). This will prove to be an important property.

While a downward continuation of the surface winds along cylinders is dynamically reasonable in the upper region where the velocity remains constant, it is more questionable at the radii where the wind velocity decreases. For example, Wulff et al. (2022) find that here wind structure is more radially aligned in their numerical simulations. In order to disentangle the effects of the latitudinal zonal wind structure and the assumed radial decay we have also performed one simulation where we assume solid body rotation and multiply this with the depth profile Q for flow model U6:

$$U(r,\theta) = U_o \, Q(r) \, sin(\theta)$$

where U_o is the peak velocity at the outer boundary. Using the conductivity σ_F, the model is called U6SF_SBR and is listed in row 7 of Table 2. The zonal flow is prograde and the amplitude U_o has been chosen to yield a maximum magnetic Reynolds number of $\text{Rm}_{max} = 26$.

The simplified zonal flow models assume that the amplitude keeps on decaying rapidly with depth and practically vanish within the shell explored here. While the gravity data indicate a significant drop in amplitude, they do not require the flows to vanish. Figure 2 also shows the magnetic Reynolds number for a rather slow velocity of 1 cm/s (dotted line), a typical estimate based on scaling laws (Gastine et al., 2014). The respective Rm starts to dominate the zonal-flow based values below radii between 0.95 R_J and 0.93 R_J, depending on the assumed flow model, and it reaches $\text{Rm} = 10^3$ at 0.90 R_J. This suggest that there is a huge potential for magnetic action beyond the simple flow models assumed here. We will ignore these issues for our simulations but discuss possible implications in Section 4.

In the instant background field approach we keep the radial field imposed at the lower boundary constant in time. To access whether this is a reasonable assumption we have to estimate the time scale of the background field. Scaling exercises suggest a typical convective velocity of about $U_b \approx 1$ cm/s in Jupiter's interior (Gastine et al., 2014; Yadav et al., 2013). This is 15,000 times slower than the zonal winds at cloud level. The inner dynamo time scale $\mathcal{T}_b$ can be estimated by assuming that the field is advected by the convective flow (Christensen & Tilgner, 2004; Lhuillier et al., 2011). This yields

$$\mathcal{T}_b = \frac{2\pi R}{U_b \ell}, \tag{11}$$

where R is a typical radius and ℓ is the degree of the magnetic field contribution in question. Using $R = R_J$ then gives $\mathcal{T}_b \approx 1\,400/\ell$ yr. For the largest spherical harmonics degree $\ell = 10$ in our background field JRM09 we thus estimate a typical time scale of about $\mathcal{T}_b(\ell = 10) \approx 150$ yr.

In the simulations, the quasi-steady state is asymptotically approached over time. Even in the case U6SF with the most drastic changes of the background field, most of the dynamics happens during the first 10–20 years (see

a) JRM09

b) U6SF

c) U6SL

d) U6SF_SBR
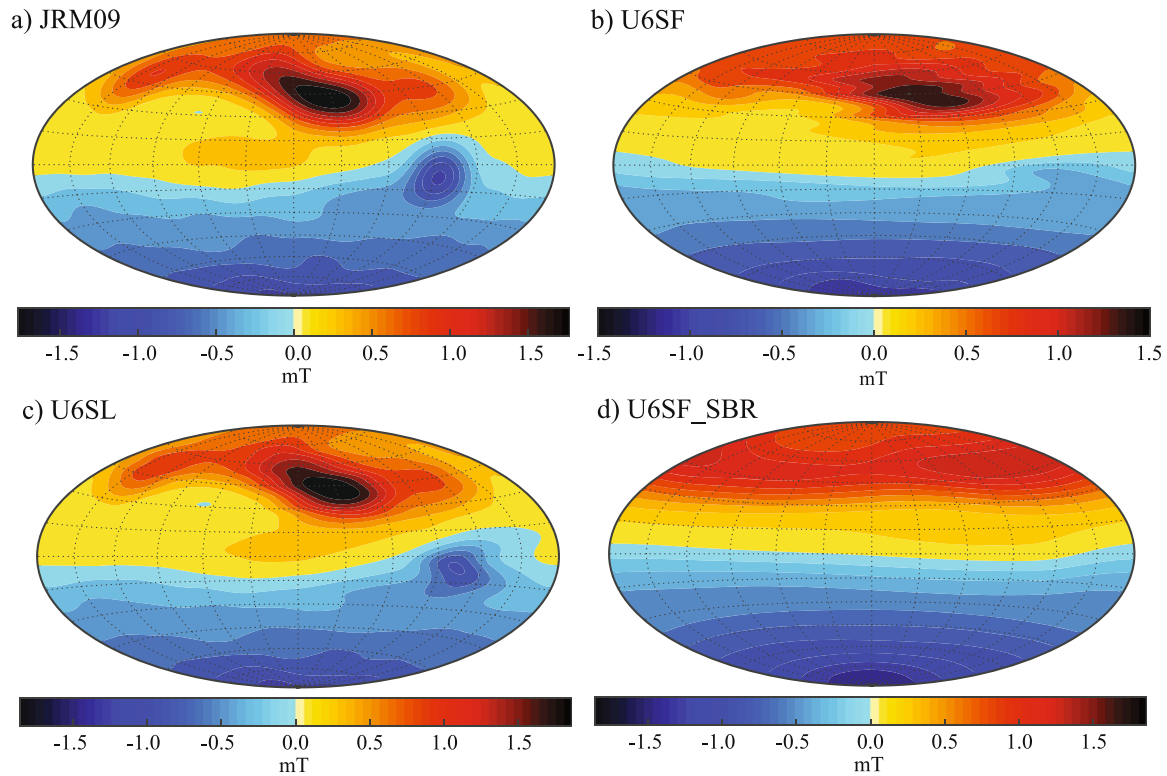
Figure 6. Radial magnetic field at planetary surface for JRM09 (a) and after 50 years of zonal flow U6 action with conductivity σ_F (b) and conductivity σ_L (c). Panel (d) shows the simulation when using conductivity σ_F and the flow model U6 but without latitudinal shear. While JRM09 is shown to degree 10, the simulations are truncated at degree 85. Yellow/red (blue) indicates radially outward (inward) field.

Figure 5). We thus estimate the time scale required to reach a quasi-steady state to about $\mathcal{T}_q \approx 10$ yr, and it can be significantly lower for the other cases. This seems to be sufficiently shorter than $\mathcal{T}_b$ to warrant the assumption of a constant background field. Note, however that the SV continues to decrease over the simulation.

When using the emerging background field approach, the field imposed at the lower boundary first has to diffuse upward. Figure 3 illustrates this process. When the lower boundary is assumed at $r_i = 0.90\,\mathrm{R_J}$, the fields takes very long to reach the surface, several centuries for σ_L and some millennia for σ_F (though we did not integrate that long). For $r_i = 0.92$, the diffusion time is much shorter, merely decades for σ_F and around a century for σ_L. We thus only perform simulations with emerging initial field for $r_i = 0.92$. Background field contributions that vary faster than the time required for the upward diffusion are filtered out by a magnetic skin effect. Consequently, the SV observation reported for Jupiter (Bloxham et al., 2022; Connerney et al., 2022; Moore et al., 2019) cannot originate from any dynamo dynamics below $r_i = 0.90\,\mathrm{R_J}$.

3. Simulation Results

3.1. Approaching the Quasi-Stationary State

The zonal flow action advects the background field and thereby induces electric currents. Since the related magnetic diffusion seeks to balance the advection, the system asymptotically approaches a quasi-steady state. The zonal flows only act on the non-axisymmetric field, and the balance is to a large part achieved by reducing these components, that is, the induced field opposes the non-axisymmetric background field. The magnetic Reynolds number is a measure for the induced field required to reach the quasi-steady state. The flow amplitude determines the rate of field modification.

Figure 4 compares the radial profiles of the rms contributions to the radial induction equation for $t = 0.1$ year (top), $t = 10$ years (middle), and $t = 50$ years (bottom). For the shallow profile U1 (left panels), where Rm remains always below 0.11, the fast flow in the outer region very effectively establishes a balance. At $t = 0.1$ year,the SV (black), which is initially dominated by the fast flows close to the surface, has already been reduced by up to three
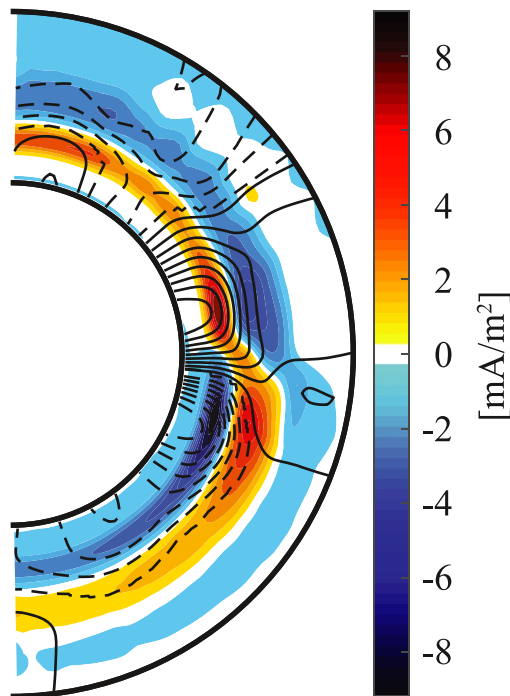
Figure 7. Meridional cut slicing through the Great Blue Spot (90° longitude). Shown is model U6SF at $t = 50$ years. Note that the model covers the region between 0.90 R_J and 0.98 R_J, but we have linearly stretched the radius to increase visibility. The fieldlines ignore the longitudinal field component. Color contours show prograde (retrograde) longitudinal electric currents in yellow to red (blue).

orders of magnitude. The advection profile (red) roughly reflects the decay of the zonal flow amplitude with depth. At around $r = 0.955$ R the flow amplitude becomes so small that diffusion (blue) starts to dominate the SV. Below this radius, the currents simply diffuse to greater depth.

At $t = 10$ years, the SV has been reduce by up to five orders of magnitude and diffusion dominates for $r \leq 0.94$ R. It takes another 40 years to reduce the SV by another order of magnitude. The growing cancellation between advection and diffusion continuously slows down the evolution.

The respective behavior for the deep flow model U6 is illustrated in the right panels of Figure 4. The scenario is similar to that for U1, but the cancellation seems less effective. After $t = 0.1$ year, the SV has been reduced by a bit more than one order of magnitude compared to nearly three orders of magnitude for U1. Also, diffusive effects seem to be less important at depth for U6 than for U1. The larger Rm means that larger induced fields are required to reach the quasi-steady state. Since flow and background field are the same, however, the rate of flow production remains identical to the U1 simulation. The cancellation is thus less effective and takes longer. As we will discuss below, the larger Rm for U6 also means that the magnetic field is significantly modified during the dynamic evolution, which reduces the effectiveness of the advection and therefore further slows down the evolution.
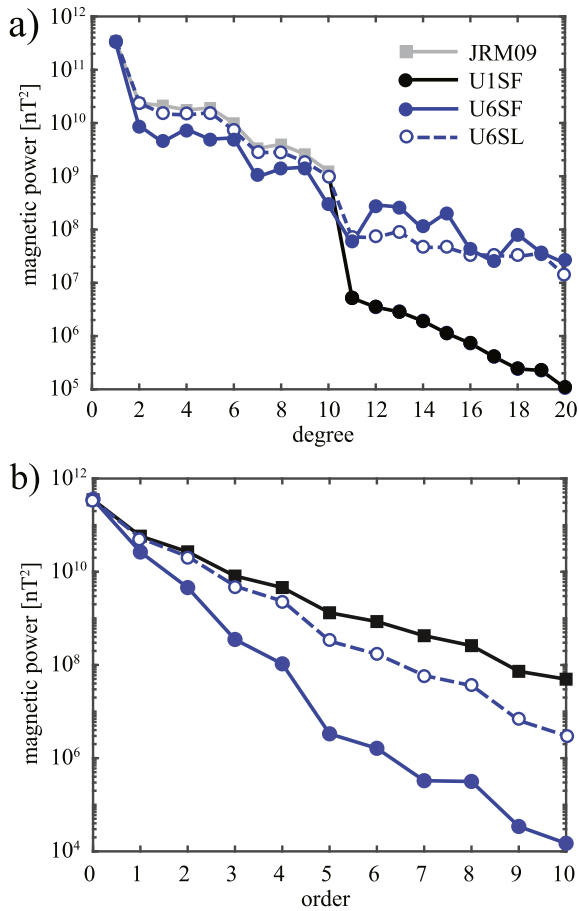
The asymptotic behavior of the progressive cancellation is illustrated in Figure 5, which shows the evolution of the SV (panel a) and the rms field strength B (panel b) at the outer boundary (solid lines) and mid radius (dotted lines) in the shell. For flow U1 (black), the decay in SV happens indeed much faster than for U6 (blue), but the overall behavior is similar. The smaller induced field required for the cancellation is too small for U1 to be discernible in Figure 5b; the rms field strength seems to remain unaffected. For flow U6 with Rm values up to 22, the induced currents are much stronger and significantly change the overall magnetic field, reducing its amplitude at the outer boundary by more than 40%.

3.2. Changes in Field Structure

Figure 6 illustrates the changes in the radial surface field, comparing JRM09 (panel a) with the modified field after $t = 50$ years of U6 action for both conductivity models. The modifications are strongest where fast zonal flows act on non-axisymmetric field, a combination most eminent around the GBS. For the higher conductivity model σ_F (panel b), the resulting field is much more axisymmetric than JMR09 and the GBS has basically been wiped out. For σ_L, on the other hand, the attenuation of non-axisymmetric features is less effective and the GBS remains reasonably pronounced. A secondary effect is the small scale latitudinal distortion or feathering induced by the latitudinal shear in the zonal flow. This is mostly apparent in the northern hemisphere for σ_F in panel b) of Figure 6. For σ_L, on the other hand, the most obvious respective modification is a distortion of the shape of the GBS. These distortions are mostly represented by spherical harmonic contributions beyond degree $\ell = 10$. When restricting the field to $\ell \leq 10$, like in our JRM09 model, the shape of the GBS seems largely unchanged (not shown).

The attenuation of the non-axisymmetric field is not directly caused by latitudinal zonal-wind shear but rather by the strong radial gradient in induction due to the steep gradients in flow and electrical conductivity. Our simulation U6SL_SBR, shown in panel d) of Figure 6, illustrates this point. The model uses the same electrical conductivity and the radial flow decay as in U6SF but assumes a constant rotation at any radius. Consequently, there is no latitudinal shear and the feathering is missing. However, the attenuation of non-axisymmetric field structures is even somewhat stronger than before, in particular in the northern hemisphere. Also notable is the stronger eastward advection due to the consistent eastward flow. Important for the degree of the attenuation is the correlation of zonal winds and non-axisymmetric features at depths where the magnetic Reynolds number reaches its maximum, as we will further discuss below. While the zonal flow velocities are comparable around the

Figure 8. Comparison of the magnetic power spectra of JRM09 (gray) with the spectra after 50 years of zonal flow action for flow model U1 (black) and model U6 (blue). For U6 results for σ_F (solid, filled symbols) and σ_L (dotted, open symbols) are shown. Spectra for U1 are virtually identical to JRM09.

equator, their rms value is about an order of magnitude larger in model U6SF_SBR than in model U6SF at latitudes where the pronounced non-axisymmetric northern feature resides.

The dynamics behind the field changes is further illustrated in Figure 7, which shows the fieldlines and contours of the longitudinal electric currents after $t = 50$ years in model U6SF. For plotting the fieldlines we ignored the longitudinal magnetic field component and we have chosen a meridional cut that slices through the GBS. The currents are purely toroidal, which means that they have no radial component and close on spherical shells. The figure shows a double currents sheet, which is typical for our simulations and slowly moves inward with time. The outer current layer marks where advection induces the strongest currents. The magnetic field produced by this currents opposes the non-axisymmetric components of the background field, resulting in the much more axisymmetric field at the surface. The lower current layer, where the currents flow in the opposite direction, results from the fact that the advection in the outer layer drags the field through this region. The resulting time dependence dominates the current production. The boundary between both layers is roughly located at the depth where dissipation starts to dominate advection in Figure 4.

Figure 8 compares magnetic power spectra of JRM09 (gray) with the respective spectra after 50 years of zonal flow U1 (black) and U6 (blue) action. Since Rm remains small for U1 the spectrum is virtually identical with the one for JRM09 at $\ell \leq 10$. The latitudinal complexity of the zonal flow leads to the induction of additional small amplitude field contributions beyond $\ell = 10$, the maximum JRM09 degree used here.

The situation is very different for the deeper flow model U6 with $\mathrm{Rm}_{max} = 22$. Panel b) in Figure 8 shows that the non-axisymmetric contributions of JRM09 are significantly reduced, an effect that increases with spherical harmonic order m. For conductivity σ_F, the power in the $m = 1$ harmonics is decreased by less than a factor 2, while the power in the $m = 10$ field is reduced by more than three orders of magnitude. For conductivity σ_L, the power reduction is significantly lower, remaining rather weak for $m \leq 5$ and rising to a bit more than an order of magnitude for $m = 10$. The newly induced harmonics beyond $\ell = 10$ contribute more significantly to the overall field than for the shallow flow U1. Naturally, these harmonics have no axisymmetric contributions. Since Jupiter's magnetic field is dominated by non-axisymmetric contributions for $\ell > 1$ the significant reduction of the non-axisymmetric field also strongly affects the degree spectrum shown in panel a) of Figure 8.

The updated Jupiter field model JRM33 offers reasonably well constrained harmonics up to degree and order 13. Generally, JRM33 and JRM09 yield a very similar field structure. Slight differences are, for example, the somewhat more confined banded patch of outward directed radial field in the northern hemisphere of JRM33 and the somewhat different form of the GBS. Figure 9 illustrates that the attenuation of the GBS is therefore slightly stronger for JRM33 than for JRM09.

Our analysis shows that the attenuation of non-axisymmetric field components is the main effect of zonal flows. All simulations with instant background field have been integrated for at least 50 years. At this point they have reached a quasi-stationary state where the field structure changes only very slowly. Column 9 in Table 2 list the decay rate of the radial field at the end of the integration, expressed as relative decay of the background field over 100 years. The largest value is only 2.6%.
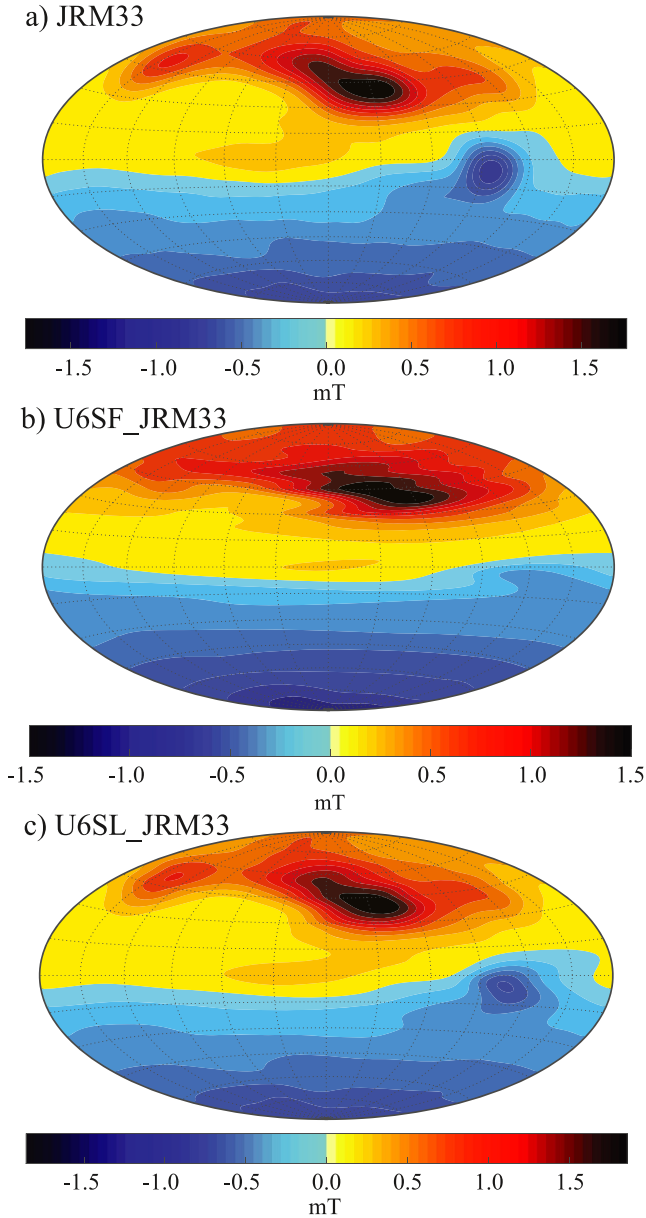
We have also run five simulations with emerging background field. Figure 10 compares the surface field structures at different times for the emerging background field with the instant background field solution already shown in Figure 6. Since we solve a linear system, the results also apply to individual features, for example, a GBS appearing on top of an already existing background field. The zonal wind effects on the field are very similar for both initial conditions. However, the overall field amplitude remains lower in the emerging field case until the

Figure 9. Radial magnetic field at planetary surface for JRM33 (a) and after 50 years of zonal flow U6 action with conductivity σ_F (b) and conductivity σ_L (c). While JRM33 is shown to degree 13, the simulations are truncated at degree 85. Yellow/red (blue) indicates radially outward (inward) field.

imposed field had enough time to diffuse to the surface. After 100 years (panel c), the field is still about 20% weaker than in the instant case (panel a) but practically reaches the same strength after 150 years (not shown).

The diffusion from the lower boundary to the surface leaves the field structure largely unchanged. The reason is that radial diffusion rather than horizontal diffusion clearly dominates. Any structural change is due to the zonal wind action and thus very similar for both instant and emerging background field.

Figure 11 compiles the relative attenuation of non-axisymmetric field B'_r,

$$\Delta b = \left(B'_b - B'\right)/B'_b, \tag{12}$$

as a function of the maximum magnetic Reynolds number Rm_{max}. The field reduction is roughly proportional to Rm_{max} with a proportionality factor of about 0.02 (black line). We can identify these changes with the locally induced field B_I. Once the balance between advection and diffusion roughly holds, the rms strength of the radial B_I can be estimated via (Wicht, Gastine, Duarte, et al., 2019)

$$\frac{UB'_b}{d_\phi} \approx \lambda \, \frac{B_I}{d_\lambda^2}, \tag{13}$$

where d_ϕ is the typical azimuthal length scale of the background field. We have assumed here that d_λ is the smallest length scale that maximizes dissipation. For very steeply decaying zonal flows, the respective scale hight may actually become smaller than d_λ. In our models this may only happen in the region $r < 0.95$ and thus has little impact on Rm_{max}. Equation 13 assumes that B_I would not contribute to the induction term, which is obviously not correct for our simulations with higher Rm_{max}.

Equation 13 suggest that

$$B_I \approx Rm \, \frac{d_\lambda}{d_\phi} \, B'_b, \tag{14}$$

similar to the relation already introducing in Equation 4. Consequently, we would expect

$$\Delta b \approx B_I/B'_b \approx Rm \, \frac{d_\lambda}{d_\phi} = \frac{U d_\lambda^2}{\lambda \, d_\phi}. \tag{15}$$

At latitudes of Jupiter's GBS, length scale d_ϕ is around 0.3 R_J while d_λ is about 3×10^{-3} at the depth of interest here ($0.94 < r/R_J < 0.97$); see Figure 1b. The length scale ratio is thus about $d_\lambda/d_\phi \approx 10^{-2}$, which is close to the factor 0.02 suggested by Figure 11. The fact that we can use Rm_{max} in Figure 11 indicates that the most active region in the induction process is where Rm reaches its maximum.

3.3. Secular Variation

We have already discussed how magnetic diffusion progressively cancels advection and that the active region of ongoing cancellation moves deeper into the shell over time. This bears the question whether the SV that could potentially be observed at the surface reflects the zonal flow at a radius $r_U(t)$ at a given time. The fact that the latitudinal structure of the cylindrical flow changes with depth provides a possibility to constrain $r_U(t)$.
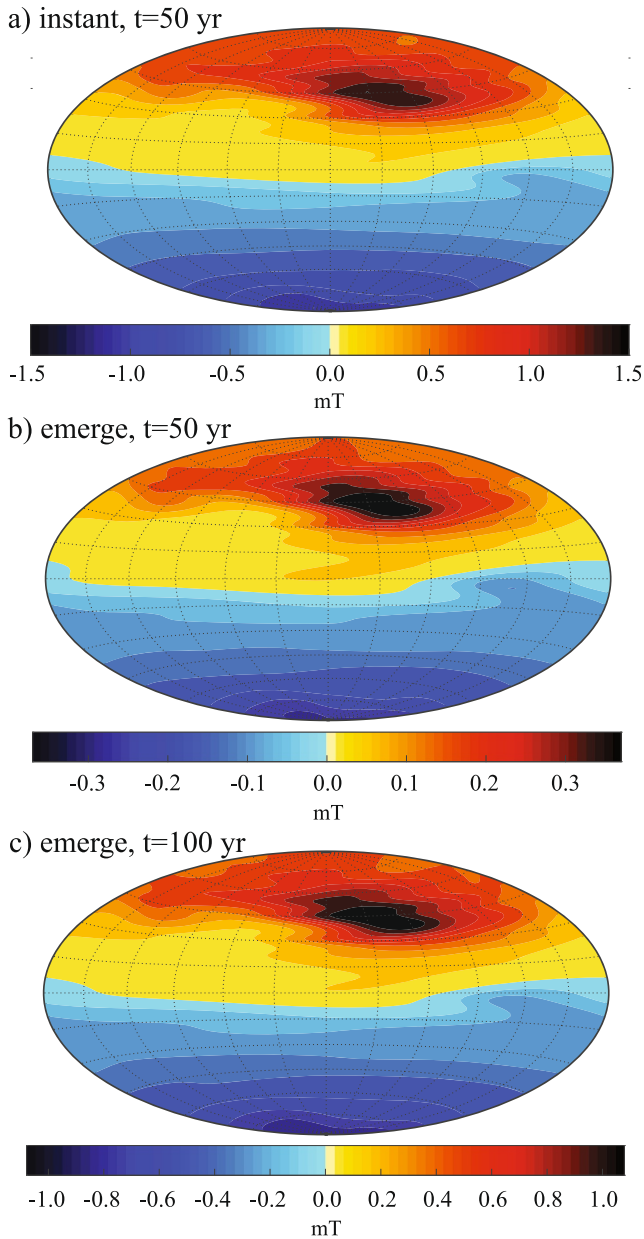
Figure 10. Radial magnetic field at planetary surface for flow U6 and conductivity σ_F. Panel (a) shows the result for an instant background field while the other two panels show the field with an emerging background field after $t = 50$ years (b) and $t = 100$ years (c). Yellow/red (blue) colors indicates radially outward (inward) field.

The advection causes a drift of the non-axisymmetric field in longitudinal direction, which can be described by

$$B_r(r,\theta,\phi,t) = \sum_m B_m(r,\theta,t) \exp(i\,m\,[\phi - ct]), \tag{16}$$

where $B_m(r, \theta, t)$ denotes the contribution of spherical harmonic order m, which depends on latitude and radius and may grow or decay over time. Drift frequency c also likewise depends on radius, latitude, and time. We calculate $c(r, \theta, t)$ from B_m at times t and $t + \Delta t$, typically choosing $m = 1$ and a Δt in the order of 10^{-3} yr (a few time steps). Experiments using other wave numbers and Δt verified the robustness of the method.

In order to quantify the similarity of the magnetic drift velocity,

$$U_c(r,\theta,t) = r \sin\theta\, c(r,\theta,t)\, \frac{R_J}{r}, \tag{17}$$

and the rescaled zonal flow velocity at radius r,

$$U_Z(r,\theta) = U(r,\theta)\, \frac{R_J}{r}, \tag{18}$$

we simply compare the rms amplitudes. The additional factor R_J/r in Equation 17 and Equation 18 accounts for the spherical geometry. Since the zonal flow action is mostly concentrated around the region of the GBS, we analyze velocities averaged between $\theta_1 = 80°$ and $\theta_2 = 110°$ and refer to the respective values as $\overline{U}_c(r)$ and $\overline{U}_Z(r)$, respectively.

To quantify the similarity of the latitudinal structure of surface drift and zonal flow at depth we calculate the Pearson correlation coefficient P at a given time:

$$P(r) = \frac{\langle (U_c(R_J) - \langle U_c(R_J)\rangle)\,(U_Z(r) - \langle U_Z(r)\rangle)\rangle}{\langle U_c(R_J)) - \langle U_c(R_J)\rangle\rangle\,\langle U_Z(r) - \langle U_Z(r)\rangle\rangle}, \tag{19}$$

where the triangular brackets denote a latitudinal mean.

Figure 12 illustrates the evolution of U_c in models U1SF, U6SF, and U6SL. The left column compares radial profiles of drift $\overline{U}_c$ at different times with the mean zonal flow $\overline{U}_Z$. $\overline{U}_Z$ is prograde for shallow depths where the prograde equatorial jet rules. It becomes retrograde once the first flanking retrograde jets dominate below $r \leq 0.98\ R_J$ and once more changes sign at $r \leq 0.955\ R_J$ where the second prograde flanking jets start to dominate our particular latitudinal mean. The averaged drift $\overline{U}_c$ is always roughly constant over the depth region where the balance between advection and diffusion, illustrated in Figure 4, has been achieved to a higher degree. It decreases with time as the balance becomes more and more perfect.

The Pearson correlation coefficients, shown in the right column of Figure 12, indicate the active advection radius r_U of the zonal flow responsible for the drift. For the shallow flow model U1 in combination with conductivity σ_F (top row), the drift pattern is at all times determined by the zonal flow around the radius $r_U = 0.966$, the depth where Rm reaches its maximum. The drift is therefore always retrograde. Since Rm_{max} is rather small, the balance between advection and diffusion is reached very quickly. After only $t = 0.1$ year, the drift velocity has already been reduced to about 10^{-2} m/s and rapidly drops further, reaching about 10^{-3} m/s after one year. These results
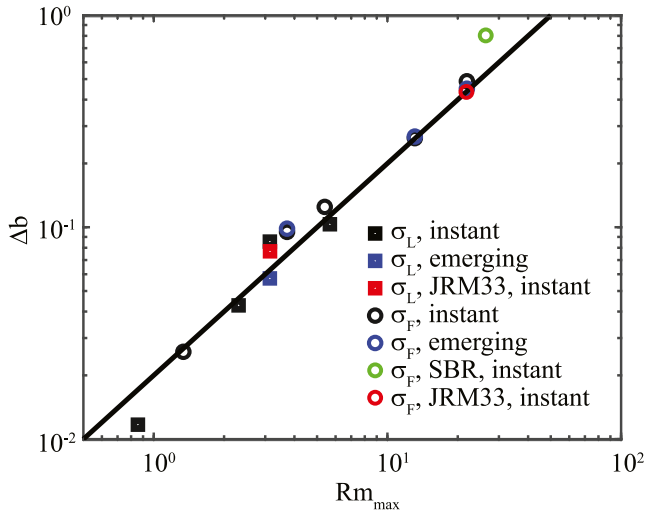
Figure 11. Dependence of the relative reduction Δb of non-axisymmetric radial field on the maximum magnetic Reynolds number Rm_{max} for all models. All models assume a Jupiter-like latitudinal surface flow structure, except one model indicated by the green circle (model 8 in Table 2). Red symbols indicate the two simulations that use JRM33 instead of JRM09 as a background field (models 7 and 14 in Table 2).

show that r_U does not coincide with the depth of the electric currents layers discussed above but is more closely related to the depth where Rm reaches its maximum.

Figure 13 compares the Jupiter SV model DRF from Bloxham et al. (2022) (panel a) with the surface SV in the simulations at $t = 10$ years (panel b). At all times, the drift for model U1SF is clearly dominated by a retrograde drift of the GBS, which at this time is already as slow as 10^{-4} m/s.

For the deep flow model U6 and the same conductivity σ_F (middle row of Figure 12) Rm reaches its maximum at $r = 0.940$ R_J and the GBS drift is always prograde. After about 10 years, its amplitude lies within the range of values proposed for Jupiter (gray bar in Figure 12) for about four decades. The stronger magnetic field modulations, however, yield a very complex SV pattern shown in Figure 13d where shearing of the background field and diffusion contribute significantly. The relative contribution of drift to the total SV decreases continuously and amounts to only about 10% at $t = 50$ years. The P value therefore also decreases over time and its maximum moves deeper, as is demonstrated in the middle row of Figure 12.

Using the same flow model U6 but the lower conductivity σ_L yields results that lie between the two extremes just discussed. The lower row of Figure 12 shows that the drift is always prograde and for about two decades has an amplitude within the range suggested for Jupiter (gray bar). Panel c) in Figure 13 shows the SV map after $t = 10$ years. At this time the rms drift amounts to only about 30% of the total SV. Additional SV contributions are clearly visible and yield a more diffused and distorted pattern around the GBS. This distortion reflects spherical harmonic contributions $\ell > 10$. When restricting the resolution to $\ell \leq 10$ the shape of the two dominant SV patches is much more roundish (not shown).

Figure 14 compares the respective surface drift velocity (black) with the zonal flow at a depth of $r = 0.945$ R_J (blue) where $P \approx 0.8$. The zonal flow has been reduced by a factor of $1/250$ to account for the cancellation between advection and diffusion. The comparison suggests that the diffusion has filtered out smaller scale latitudinal variations, resulting in a purely prograde drift. An observed surface drift could thus potentially provide a large-scale representation of the zonal flow pattern at depth but will underestimate the flow amplitude by orders of magnitude.

The fast prograde drift just north of the equator goes back to the downward continued fastest prograde surface jet around 25° northern latitude. This is partly responsible for the distortion of the GBS seen in Figure 6. Also shown in Figure 14 are the two SV models by Bloxham et al. (2022). The SBFR-2 model (green) assumes a solid body rotation, while model DRF (red) allows for additional lateral variations. Both are roughly similar to our simulation results but there are also differences. While the drift velocity is particularly low in the northern hemisphere in our models, DRF suggests a lower velocity in the southern hemisphere. Note, however, that the lack of non-axisymmetric field structures south of the GBS yields a low SV signal and this potentially complicates the inversion for flows.

When using the emerging initial field condition, the secular variation is always dominated by the imposed linear field growth and by the diffusive field emergence. The SV has thus no similarity with the observations. For model *U1SFe*, the JRM09 pattern remains basically unchanged but gradually increases in amplitude until reaching its full strength after about 150 years. For model *U6SFe*, the GBS and other non-axisymmetric field components are quickly attenuated after a few years. The smoothed field then also gradually increases, as is demonstrated in Figure 10. Zonal flow advection may become more prominent in the SV of these cases when increasing the time scales of the background field, for example, by putting the lower boundary at $r_i = 0.9$ R_J rather than $r_i = 0.92$ R_J like in our simulations (see Figure 3).

4. Discussion

Our analysis demonstrates that the action of downward-continued surface zonal winds on the structure of the deep dynamo field has two effects. First, the flow imprints its latitudinal structure. Significantly stronger, however, is the
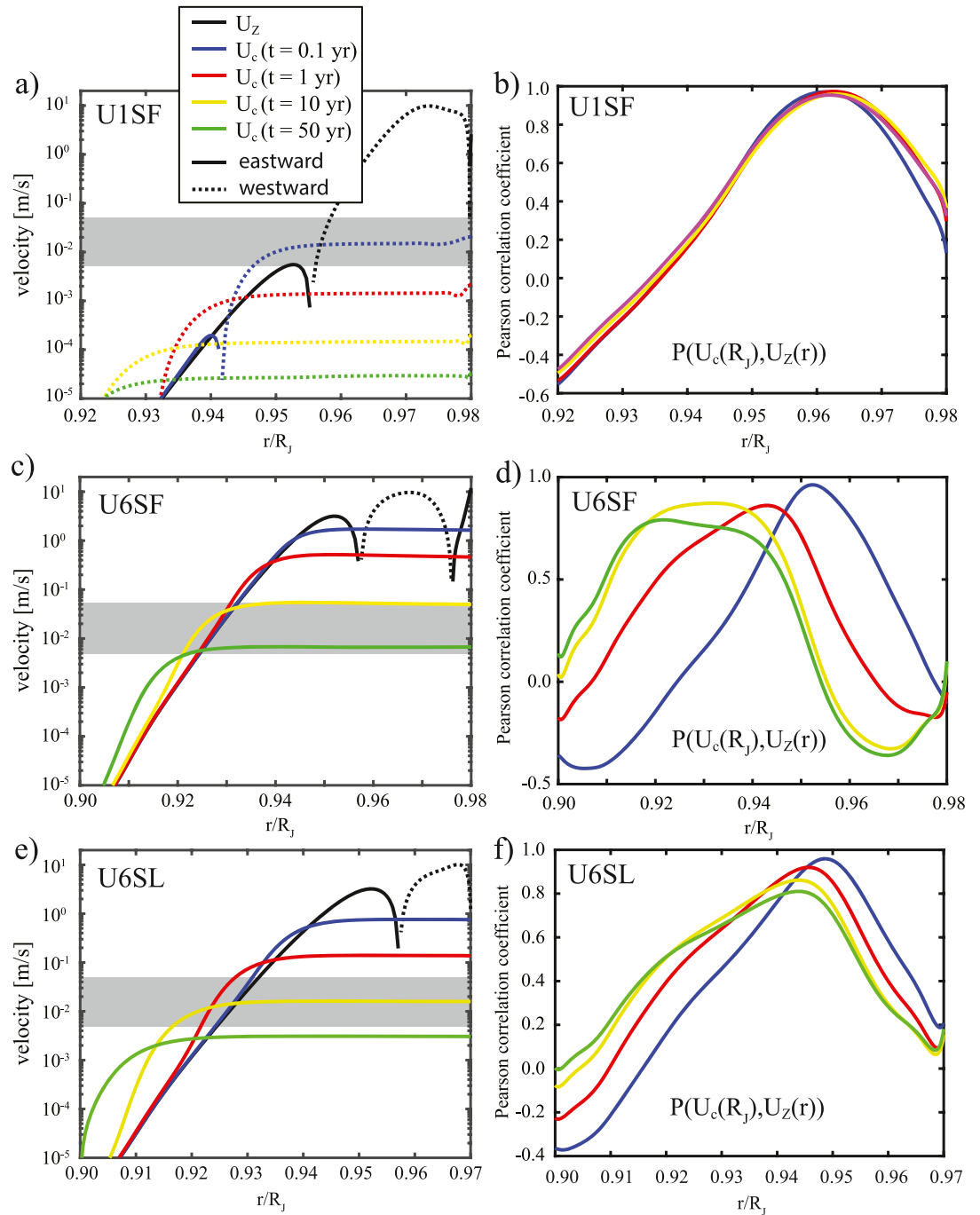
Figure 12. The left column shows the rms drift velocity $\overline{U}_c$ in the vicinity of the Great Blue Spot (GBS) for different models at various times. The black line gives the actual flow velocity, averaged over the latitude range of the GBS. Full (broken) lines indicate eastward (westward) drift. The right column shows the respective Pearson correlation coefficients between surface drift velocity and zonal flow velocity. The gray bar (left column) indicates the range suggested by observations (Bloxham et al., 2022; Connerney et al., 2022; Moore et al., 2019).

second effect, the attenuation of non-axisymmetric field contributions. The attenuation relies on the strong radial gradient in magnetic induction and is largely independent of the particular latitudinal flow structure at depth.
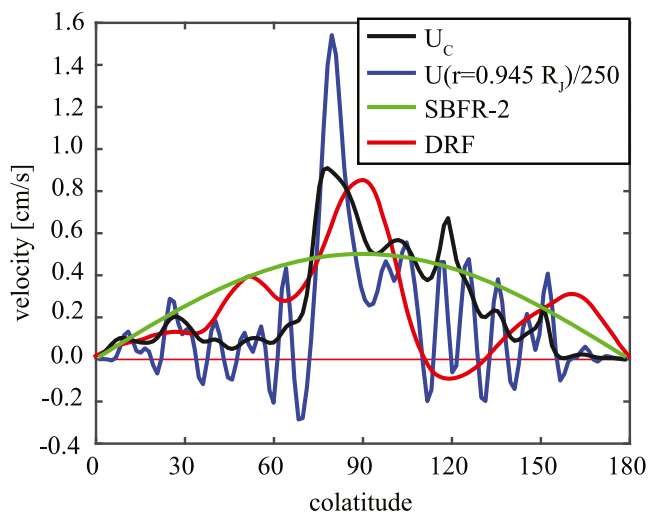
The attenuation provides a new constraint on the depth of the zonal winds, or more precisely on the local magnetic Reynolds number. Assuming that the GBS indeed originates from a deeper dynamo region we can dismiss model
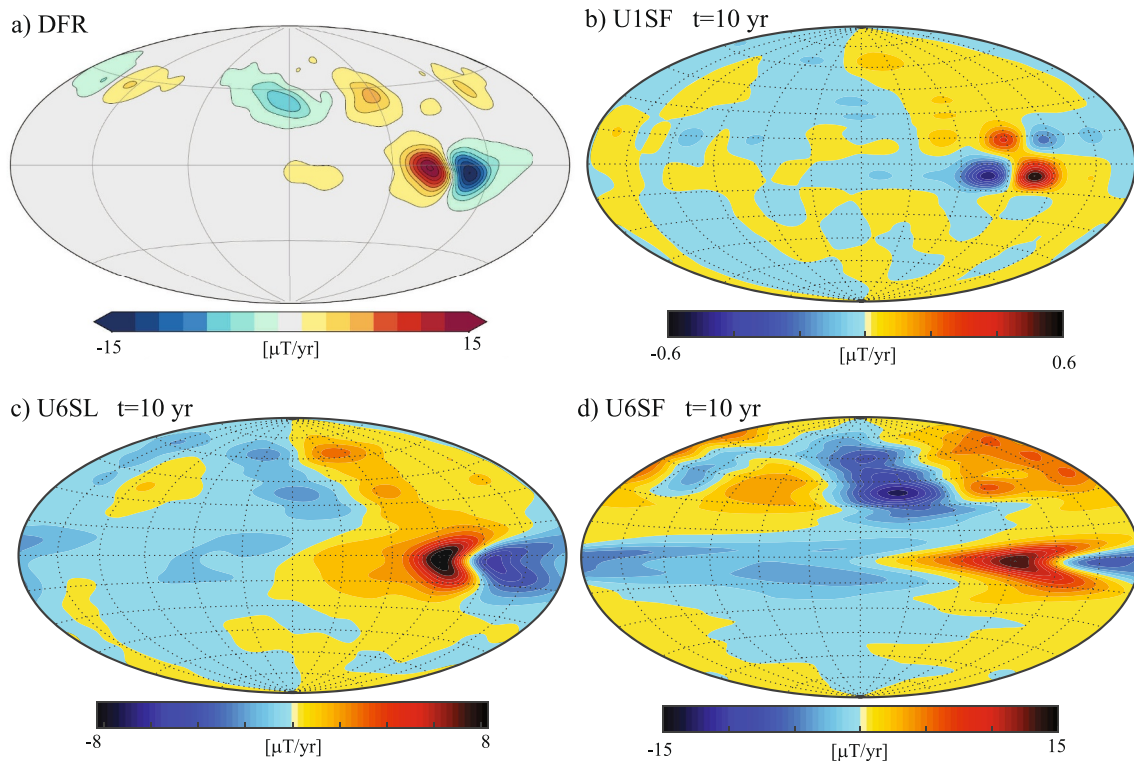
Figure 13. SV at planetary surface: DRF by Bloxham et al. (2022) (a), model U1SF (b), model U6SF (c), and model U6SL (d). All models use the instant background field initial condition and are shown after 10 years of integration.

U6SF, the deep flow U6 in combination with σ_F (Figure 6b), since it would leave little observable trace of the GBS. When using the lower conductivity model σ_L, however, the GBS is somewhat attenuated and distorted but remains clearly identifiable (Figure 6c). This model therefore seems a viable option, provided the GBS is even more intense and has a somewhat different shape at depth than at the surface. Expressed in terms of the maximum local magnetic Reynolds number in a model, values of $Rm_{max} > 10$ must be dismissed while values $Rm_{max} < 5$ seem still possible.

Figure 15 illustrates how Rm_{max} depends on the flow parameters H and δ. The solid and broken black lines mark the value $Rm_{max} = 3$ for σ_F and σ_L respectively. Parameter combinations close to or to the left (or below) of these lines seem possible since they retain the GBS as a distinct and compact feature. This includes slowly decaying flow profiles with $\delta > 500$ km, which we have not explored in our simulations. In the first paper based on Juno gravity data, Kaspi et al. (2018) suggest a profile with $H = 1,800$ km and $\delta = 1,570$ km. Such an extreme case would yield a large Rm_{max} value beyond 10^2 and must therefore be dismissed. However, for example the combination $H = 1800$ km and $\delta = 700$ km seems still compatible with our new constraint. Our flow model $U6$ with $H = 2,500$ km and $\delta = 500$ km is close to the deepest reaching acceptable flow for the conductivity model σ_F.

Figure 14. Comparison of the surface drift velocity U_C after 25 years in simulation U6SL with the zonal flow profiles at $r = 0.945 \, R_J$. The zonal flow has been divided by 250 to mimic the cancellation. Also shown are the two SV models suggested by Bloxham et al. (2022).

The differences to the model U1 by Galanti and Kaspi (2021), which was also constructed to satisfy magnetic observations, are significant. For U1 the depth where the rms flow amplitude has decreased by one order of magnitude is about $D = 2,300$ km. For U6 this is more than 1,000 km deeper with $D = 3,400$ km. Note, however, that these numbers depend on the assumed form of the decay profile Q. Generally, an even sharper decay at depth (a smaller δ in the profiles explored here) would allow for an increased depth D.
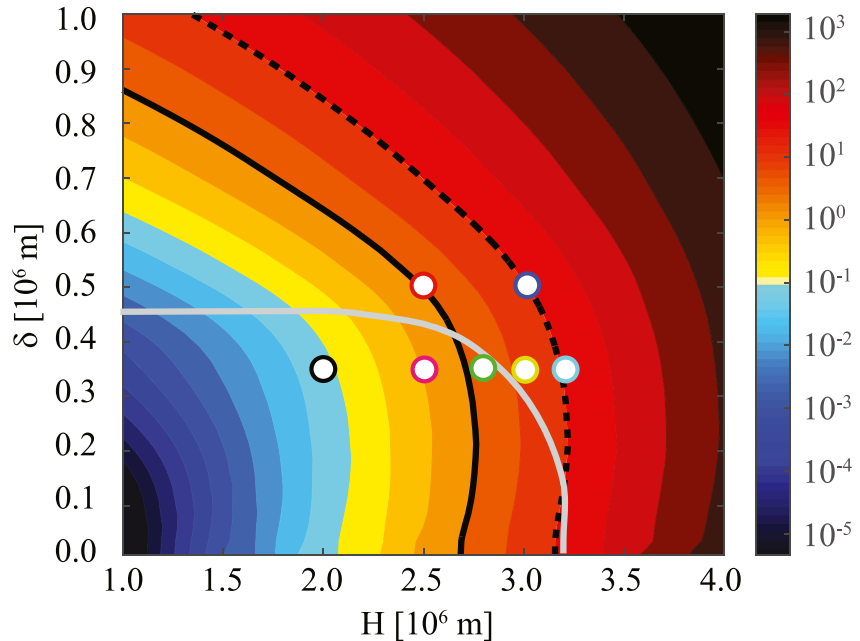
Figure 15. Dependence of the maximum magnetic Reynolds number on the flow parameters H and δ (see Equation 10). The seven flow models explored here are marked by white dots with colored rims following the color code explained in Table 1. Solid and broken black lines in indicate where $\mathrm{Rm}_{max} = 3$ for the conductivity profiles σ_F and σ_L, respectively. The background color shows the maximum magnetic Reynolds number Rm_{max} for σ_F. The gray line marks values beyond which the surface drift of the Great Blue Spot is prograde for σ_F.

The possible mechanism that prevents the winds from penetrating deeper provides additional information on the flow profile. While Lorentz forces have often been brought into play in the past, Christensen et al. (2020) suggest that a stably stratified layer is required to efficiently brake the winds. This has been supported by recent 3d numerical simulations (Gastine & Wicht, 2021; Wulff et al., 2022). Christensen et al. (2020) show that a rather abrupt decay in the layer over $\delta = 150 - 300$ km is typical in this scenario. When concentrating on our steeper profiles with $\delta = 350$ km, maximum depths of $H = 2,500$ km for σ_F or $H = 3,000$ km for σ_L are compatible with our new magnetic criterion. This would put the top of the stably stratified layer at 0.964 R_J or 0.957 R_J respectively. Once again, the estimates depend on the assumed decay profile.

Some authors suggest that the winds observed at Jupiter's cloud level may not reflect the structure at depth. While we do not explicitly explore such a model, our results provide some general ideas that would still apply. For example, the rather shallow flows suggested by Kulowski et al. (2021) with depths below 1,500 km would yield no magnetic signal. Kong et al. (2018), on the other hand, suggest a very deep zonal wind layer down to about 0.8 R_J. The winds have a very different structure than those observed at the surface and reach maximum amplitudes of a few meter per second at around 0.9 R_J. When using the conductivity model σ_F, these velocities would yield magnetic Reynolds number beyond 10^5 and the magnetic effects would be much stronger than anything considered here. Since only a tiny radial velocity contribution would then be sufficient to excite dynamo action, our simple model does not apply. On any account, a large part of the observed field should originate from such a layer.

The axisymmetry of Saturn's magnetic field can be explained by effects very similar to the ones discussed here. Stevenson (1980) suggest that an electrically conducting stably stratified layer sitting on top of Saturn's dynamo region could explain its peculiar magnetic field configuration. Zonal winds, which are easily excited by thermal wind effects in this layer, but also a magnetic skin effect due to magnetic field variations could conspire to heavily attenuate the non-axisymmetric field (Christensen, 2006; Christensen & Wicht, 2008). To avoid similar effects for Jupiter, the stable layer should not reach too deep. When assuming a typical wind velocity of only 1 cm/s, values of $\mathrm{Rm} \approx 5$ are reached at 0.932 R_J for σ_F and 0.921 R_J for σ_L (see Figure 2). Since these radii would mark the top of the deep dynamo region, we would expect the dynamo to start not deeper than $r_D \approx 0.92$ R_J.

Our analysis only addresses the role of zonal winds in the outer few percent of Jupiter's radius, but zonal flows in the deeper dynamo region will also influence the magnetic field structure and its secular variation. Connerney et al. (2022) suggests that the top of the dynamo is located at a radius of $r_D = 0.8 \, R_J$. This conjecture is based on the fact that the downward-continued magnetic spectrum would become white at this radius. For Earth, such an assumption successfully predicts the core-mantle boundary because the low conductivity of Earth's mantle indeed makes any magnetic field production highly inefficient. For Jupiter, however, the electrical conductivity remains already assume nearly metallic values between $r_D = 0.8 \, R_J$ and $r_D = 0.9 \, R_J$ (see Figure 1). Rather slow flows would therefore suffice to reach Rm values significant enough for strong magnetic field modifications or even dynamo action. The excessively long diffusion time is another argument against such a deep dynamo. The simulations for our emerging-field initial condition (see Figure 3) demonstrate that the field would already take several centuries to diffuse from $r = 0.90 \, R_J$ to the surface. Any faster variations in the deep dynamo would therefore be efficiently attenuated even without the zonal flow action discussed here. Since higher spherical harmonic degrees vary faster, the attenuation would strongly affect the magnetic spectrum (Gastine & Wicht, 2021). However, a detailed analysis how magnetic field variations originating in the dynamo region are modified before becoming observable at Jupiter's surface is still missing.

Our analysis also only applies to zonal winds that remain steady on time-scales of decades to centuries. The main jets seen at Jupiter's surface fulfill this criteria but faster small-amplitude variations of the zonal winds could still be superimposed. Hori et al. (2023) suggest that torsional oscillations with time scales of up to a decade may cause observed variations in visible and infrared wavelengths. However, the high magnetic dissipation makes it unlikely that the related zonal flows would extend to the outer few percent of Jupiter's radius. Hori et al. (2023) speculate that connected variations in convective efficiency may nevertheless explain the observations.

Our results show that the degree of attenuation in the non-axisymmetric field can be estimated by the modified magnetic Reynolds number $\text{Rm}_{max}(d_\lambda / d_\phi)$. While Wicht et al. (2019b) already concluded that this parameter combination would determined the locally induced field changes, they did not envision the attenuation of the non-axisymmetric field.

When using the emerging background field initial condition, the SV is always dominated by the field diffusing to the surface and not by zonal wind effects. A magnetic field drift similar to the SV observations is only found when we use the instant-field initial condition. The latitudinal drift pattern then predominantly reflects a simplified version of the zonal wind action at the radius r_{max} where the magnetic Reynolds number reaches its maximum. To yield the observed prograde drift direction of the GBS, r_{max} should lie deeper than $0.955 \, R_J$. The gray line in Figure 15 marks the flow parameters where this is fulfilled for σ_F. Only combinations to the right of or above this line are expected to yield a prograde drifting GBS.

The drift velocity decreases over time, first quickly and then ever slower. The decrease reflects the progressive cancellation of advection and magnetic diffusion rather than the zonal wind speed at r_{max}. The original SV estimate by Moore et al. (2019) is based on four decades of observations. In order to maintain a similar drift velocity over a comparable duration Rm_{max} values of order one are necessary. Figure 15 illustrates that a prograde drift in combination with $\text{Rm}_{max} \leq 3$ requires $\delta > 400$ km, which is somewhat larger than the value suggested by Christensen et al. (2020).

5. Conclusion

We have simulated the effects of the zonal winds on a magnetic field created by a deeper dynamo, exploring different zonal wind models and two different electrical conductivity profiles. The results reveal that the main effect of the zonal winds is an attenuation of non-axisymmetric magnetic features. The maximum local magnetic Reynolds number Rm_{max} reached along the zonal flow profile can serve as a proxy to quantify this effects.

When Rm_{max} reaches values of 3 or larger, the effect is so strong that it seems not compatible with the existence of the GBS, a characteristic significantly non-axisymmetric feature of Jupiter's magnetic field. This new magnetic criterion allows for flows that reach to a depth of about 3,400 km rather than the roughly 2,300 km suggested by Galanti and Kaspi (2021). It also clearly disqualifies the earlier slowly decaying flows published by Kaspi et al. (2018).

Inverting the SV for the zonal flow properties at depth proves problematic in our simulations and seems therefore questionable for Jupiter. Secular variation is controlled by the fast progressive cancellation of advection and

diffusion. This yields a typically small and ever decreasing SV. In some simulations the SV is dominated by a prograde drift of the GBS, just like in the observations. However, this is highly model dependent. The slight correction of Jupiter's rotation rate suggested by Bloxham et al. (2022) offers a more convincing explanation. The observed SV then simply amounts to a tiny correction of the frame of reference rather than to any dynamo dynamics. Some additional latitudinal variations may nevertheless result from zonal wind action or from the dynamics in the deeper dynamo region (Bloxham et al., 2022). Additional observations by the Juno spacecraft during the extended phase of the mission will help to clarify this issue.

Appendix A

A1. Spectral Equations and Numerical Methods

We used to poloidal/toroidal decomposition of the magnetic field where the radial component is given by the poloidal potential b:

$$B_r = -\nabla_H^2\, b, \tag{A1}$$

where ∇_H^2 is the horizontal contribution of the Laplace operator. The poloidal potential is expanded into spherical surface harmonics Y_ℓ^m,

$$b = \sum_{\ell=0}^{L} \sum_{m=-\ell}^{m=\ell} b_{\ell m}(r)\, Y_\ell^m, \tag{A2}$$

with expansion coefficients $b_{\ell m}$. The surface harmonics

$$Y_\ell^m(\theta, \phi) = \hat{P}_\ell^m(\cos\theta)\exp(im\phi). \tag{A3}$$

are fully normalized orthogonal functions,

$$\int_{-1}^{1} d\cos\theta \int_0^{2\pi} d\phi\, Y_{\ell'}^{m'*}\, Y_\ell^m\ =\ \delta_{\ell\ell'}\, \delta_{mm'}, \tag{A4}$$

where the star denotes the complex conjugate and $\hat{P}_\ell^m$ are Legendre polynomials. Since the magnetic field is a real function, the complex expansion coefficients have to fulfill:

$$b_{\ell-m}(r) = b_{\ell m}{}^\star(r). \tag{A5}$$

When decomposing b into its spherical harmonic contributions $b_{\ell m}$ of degree ℓ and order m, the respective radial field is given by:

$$[B_r]_{\ell m} = \frac{\ell(\ell+1)}{r^2}\, b_{\ell m}(r). \tag{A6}$$

The radial induction equation that we solve for the poloidal field harmonics then reads

$$\frac{\ell(\ell+1)}{r^2}\frac{\partial}{\partial t}b_{\ell m} = -\left[\frac{U}{r\sin\theta}\frac{\partial}{\partial\phi}B_r\right]_{\ell m} - \lambda\,\frac{\ell(\ell+1)}{r^2}\left(\frac{\ell(\ell+1)}{r^2} - \frac{\partial^2}{\partial r^2}\right)b_{\ell m}. \tag{A7}$$

The first term on the right-hand side describes the induction and couples different spherical harmonic degrees ℓ for a given order m. All spherical harmonics orders, on the other hand, decouple and can be integrated in time independently.

The radial dependence is modeled by an expansion in Chebychev polynomial $C_n(r)$ up to a truncation N:

$$b_{\ell m}(r) = \sum_{n=0}^{n=N} b_{\ell m n} \, C_n(r). \tag{A8}$$

Choosing the N extrema of the polynomial C_{N-1} to define the radial grid points r_i has two advantages. First, it provides denser grid points where boundary conditions need to be accommodated. Second, we can use a fast cosine transform to switch from spectral to grid point representation.

The equation for at a radial grid point r_k and for the mode of degree ℓ and order m then reads:

$$
\frac{\ell(\ell+1)}{r_k^2} \frac{\partial}{\partial t} b_{\ell m}(r_k) = -\left[\frac{U(r_k)}{r_k \sin\theta} \frac{\partial}{\partial \phi} B_r(r_k) \right]_{\ell m}
$$
$$
- \lambda(r_k) \frac{\ell(\ell+1)}{r_k^2} \left[\frac{\ell(\ell+1)}{r_k^2} C_n(r_k) - \frac{\partial^2}{\partial r^2} C_n(r_k) \right] b_{\ell m n} \tag{A9}
$$

The Chebychev polynomials and second radial derivatives at all grid points r_k are precomputed.

The system is forwarded in time with a mixed implicit/explicit scheme that can be written as:

$$\mathbf{A}/\delta t \, (\mathbf{x}(t+\delta t) - \mathbf{x}(t)) = 3/2 \, \mathbf{N}(t) - 1/2 \, \mathbf{N}(t-\delta t) \; + \; \mathbf{D} \, (1/2 \, \mathbf{x}(t+\delta t) + 1/2 \, \mathbf{x}(t)). \tag{A10}$$

Here δt is the time step and $\mathbf{x}$ is an array containing all Chebychev coefficients for a mode of degree ℓ and order m and thus has the elements

$$x_n = b_{\ell m n}. \tag{A11}$$

The matrix $\mathbf{A}$ converts $\mathbf{x}$ to the radial field in radial grid space and has the elements

$$A_{kn} = \frac{\ell(\ell+1)}{r_k^2} C_n(r_k). \tag{A12}$$

Vector $\mathbf{N}$ formulates the induction term at all radial grid point:

$$N_k = -\left[\frac{U(r_k)}{r_k \sin\theta} \frac{\partial}{\partial \phi} B_r(r_k) \right]_{\ell m}. \tag{A13}$$

The matrix $\mathbf{D}$ describes the diffusive term with elements

$$D_{kn} = -\lambda(r_k) \frac{\ell(\ell+1)}{r_k^2 \, \delta t} \left[\frac{\ell(\ell+1)}{r_k^2} C_n(r_k) - \frac{\partial^2}{\partial r^2} C_n(r_k) \right], \tag{A14}$$

At each time step the following system of algebraic equation is solved:

$$[\mathbf{A}/\delta t - \mathbf{D}/2] \, \mathbf{x}(t+\delta t) \; = \; [\mathbf{A}/\delta t + \mathbf{D}/2] \, \mathbf{x}(t) + 3/2 \, \mathbf{N}(t) - 1/2 \, \mathbf{N}(t-\delta t), \tag{A15}$$

replacing the two equations for the boundaries with the appropriate boundary conditions. A standard LU-decomposition based on LINPACK routines is used.

Since we use JRM09 up to spherical harmonic degree 10 or JRM33 up to 13 as a background fields we only have to solve for spherical harmonic orders up to $m = 10$ or $m = 13$, respectively. The degree is truncated at $L = 85$ to resolve the complexity introduced by the zonal flows. In radius we use 181 grid points and Chebychev polynomials. Resolution test have confirmed that this resolution is sufficient. A time step of $\delta t = 5 \times 10^{-4}$ yr has been used to resolve the action of the fast zonal winds.

A2. Flow Smoothing

To arrive at a flow model used in our simulations, we first downward continue the observed flow at cloud level, assuming it remains constant on cylinders with radius $s = r \sin \theta$. This results in a flow U_0' which still contains fine-scale latitudinal structure that may reflect only shallow surface features. In addition, the downward continuation results in discontinuities at the equator. We therefore smooth the flow in two steps. First, the rotation rate $U_0'/\sin \theta$ is expanded into Legendre polynomials up to degree 60 at each radial level:

$$\omega_\ell(r) = \int_{-1}^{1} d \cos \theta \; U_0'(r,\theta)/\sin \theta \; \hat{P}_\ell. \tag{A16}$$

We solve the integrals using Gauss-Legendre quadrature. The back-transform,

$$U_0 = \sin \theta \sum_{\ell=0}^{60} \omega_\ell(r) \; \hat{P}_\ell, \tag{A17}$$

then provides the latitudinally smoothed profile at each radius. Additional smoothing in radius is applied in a second step by expanding U_0 for each latitudinal grid point in Chebychev polynomials up to degree 15. We finally arrive at the flow used in our simulations by multiply with the radial profile $Q(r)$ discussed in Section 2.2:

$$U(r,\theta) = Q(r) \; U_0(r,\theta). \tag{A18}$$

Data Availability Statement

All simulation were performed with the Matlab package SVzon, which is freely available at the repository EDMOND (Wicht, 2023). Simulation results and necessary input models can also be downloaded from the same cite.

References

Bloxham, J., Moore, K. M., Kulowski, L., Cao, H., Yadav, R. K., Stevenson, D. J., et al. (2022). Differential rotation in Jupiter's interior revealed by simultaneous inversion for the magnetic field and zonal flux velocity. *Journal of Geophysical Research (Planets)*, *127*(5), e07138. https://doi.org/10.1029/2021JE007138

Cao, H., Bloxham, J., Park, R. S., Militzer, B., Yadav, R. K., Kulowski, L., et al. (2023). Strong resemblance between surface and deep zonal winds inside Jupiter revealed by high-degree gravity moments. *The Astrophysical Journal*, *959*(2), 78. https://doi.org/10.3847/1538-4357/ad0cbb

Cao, H., & Stevenson, D. J. (2017). Gravity and zonal flows of giant planets: From the Euler equation to the thermal wind equation. *Journal of Geophysical Research*, *122*(4), 686–700. https://doi.org/10.1002/2017JE005272

Christensen, U., & Tilgner, A. (2004). Power requirement of the geodynamo from ohmic losses in numerical and laboratory dynamos. *Nature*, *429*(6988), 169–171. https://doi.org/10.1038/nature02508

Christensen, U. R. (2006). A deep dynamo generating Mercury's magnetic field. *Nature*, *444*(7122), 1056–1058. https://doi.org/10.1038/nature05342

Christensen, U. R., & Wicht, J. (2008). Models of magnetic field generation in partly stable planetary cores: Applications to Mercury and Saturn. *Icarus*, *196*(1), 16–34. https://doi.org/10.1016/j.icarus.2008.02.013

Christensen, U. R., Wicht, J., & Dietrich, W. (2020). Mechanisms for limiting the depth of zonal winds in the gas giant planets. *The Astrophysical Journal*, *890*(1), 61. https://doi.org/10.3847/1538-4357/ab698c

Connerney, J. E. P., Kotsiaros, S., Oliversen, R. J., Espley, J. R., Joergensen, J. L., Joergensen, P. S., et al. (2018). A new model of Jupiter's magnetic field from Juno's first nine orbits. *Geophysical Research Letters*, *45*(6), 2590–2596. https://doi.org/10.1002/2018GL077312

Connerney, J. E. P., Timmins, S., Oliversen, R. J., Espley, J. R., Joergensen, J. L., Kotsiaros, S., et al. (2022). A new model of Jupiter's magnetic field at the completion of Juno's prime mission. *Journal of Geophysical Research (Planets)*, *127*(2), e07055. https://doi.org/10.1029/2021JE007055

Dietrich, W., Wulff, P., Wicht, J., & Christensen, U. R. (2021). Linking zonal winds and gravity - II. Explaining the equatorially antisymmetric gravity moments of Jupiter. *Monthly Notices of the Royal Astronomical Society*, *505*(3), 3177–3191. https://doi.org/10.1093/mnras/stab1566

French, M., Becker, A., Lorenzen, W., Nettelmann, N., Bethkenhagen, M., Wicht, J., & Redmer, R. (2012). Ab initio simulations for material properties along the Jupiter Adiabat. *The Astrophysical Journal Supplement Series*, *202*(1), 5. https://doi.org/10.1088/0067-0049/202/1/5

Galanti, E., & Kaspi, Y. (2021). Combined magnetic and gravity measurements probe the deep zonal flows of the gas giants. *Monthly Notices of the Royal Astronomical Society*, *501*(2), 2352–2362. https://doi.org/10.1093/mnras/staa3722

Gastine, T., & Wicht, J. (2021). Stable stratification promotes multiple zonal jets in a turbulent Jovian dynamo model. *Icarus*, *368*, 114514. https://doi.org/10.1016/j.icarus.2021.114514

Gastine, T., Wicht, J., Duarte, L. D. V., Heimpel, M., & Becker, A. (2014). Explaining Jupiter's magnetic field and equatorial jet dynamics. *Geophysical Research Letters*, *41*(15), 5410–5419. https://doi.org/10.1002/2014GL060814

Holme, R. (2015). Large scale flow in the core. In P. Olson (Ed.), *Core dynamics, treatise on geophysics* (2nd ed., Vol. 10, pp. 91–113). Elsevier.

Hori, K., Jones, C. A., Antuñano, A., Fletcher, L. N., & Tobias, S. M. (2023). Jupiter's cloud-level variability triggered by torsional oscillations in the interior. *Nature Astronomy*, *7*, 825–835. https://doi.org/10.1038/s41550-023-01967-1

Kaspi, Y., Galanti, E., Hubbard, W. B., Stevenson, D. J., Bolton, S. J., Iess, L., et al. (2018). Jupiter's atmospheric jet streams extend thousands of kilometres deep. *Nature*, *555*(7695), 223–226. https://doi.org/10.1038/nature25793

Kaspi, Y., Galanti, E., Park, R. S., Duer, K., Gavriel, N., Durante, D., et al. (2023). Observational evidence for cylindrically oriented zonal flows on Jupiter. *Nature Astronomy*, *7*(12), 1463–1472. https://doi.org/10.1038/s41550-023-02077-8

Kong, D., Zhang, K., Schubert, G., & Anderson, J. D. (2018). Origin of Jupiter's cloud-level zonal winds remains a puzzle even after Juno. *Proceedings of the National Academy of Sciences*, *115*(34), 8499–8504. https://doi.org/10.1073/pnas.1805927115

Kulowski, L., Cao, H., Yadav, R. K., & Bloxham, J. (2021). Investigating Barotropic zonal flow in Jupiter's deep atmosphere using Juno gravitational data. *Journal of Geophysical Research: Planets*, *126*(11), e06795. https://doi.org/10.1029/2020JE006795

Lhuillier, F., Fournier, A., Hulot, G., & Aubert, J. (2011). The geomagnetic secular variation timescale in observations and numerical dynamo models. *Geophysical Research Letters*, *38*(L09), 306. https://doi.org/10.1029/2011gl047356

Liu, J., Goldreich, P. M., & Stevenson, D. J. (2008). Constraints on deep-seated zonal winds inside Jupiter and Saturn. *Icarus*, *196*(2), 653–664. https://doi.org/10.1016/j.icarus.2007.11.036

Moore, K. M., Cao, H., Bloxham, J., Stevenson, D. J., Connerney, J. E. P., & Bolton, S. J. (2019). Time variation of Jupiter's internal magnetic field consistent with zonal wind advection. *Nature Astronomy*, *3*(8), 730–735. https://doi.org/10.1038/s41550-019-0772-5

Porco, C. C., West, R. A., McEwen, A., Del Genio, A. D., Ingersoll, A. P., Thomas, P., et al. (2003). Cassini imaging of Jupiter's atmosphere, satellites, and rings. *Science*, *299*(5612), 1541–1547. https://doi.org/10.1126/science.1079462

Schwaiger, T., Jault, D., Gillet, N., Schaeffer, N., & Mandea, M. (2023). Local estimation of quasi-geostrophic flows in Earth's core. *Geophysical Journal International*, *234*(1), 494–511. https://doi.org/10.1093/gji/ggad089

Stevenson, D. J. (1980). Saturn's luminosity and magnetism. *Science*, *208*(4445), 746–748. https://doi.org/10.1126/science.208.4445.746

Wicht, J. (2023). Contributions of zonal winds to Jupiter's magnetic field structure and its secular variation: Data and Matlab code. https://doi.org/10.17617/3.CNVRWD

Wicht, J., & Gastine, T. (2020). Numerical simulations help revealing the dynamics underneath the clouds of Jupiter. *Nature Communications*, *11*(1), 2886. https://doi.org/10.1038/s41467-020-16680-0

Wicht, J., Gastine, T., & Duarte, L. D. V. (2019). Dynamo action in the steeply decaying conductivity region of Jupiter-like dynamo models. *Journal of Geophysical Research (Planets)*, *124*(3), 837–863. https://doi.org/10.1029/2018JE005759

Wicht, J., Gastine, T., Duarte, L. D. V., & Dietrich, W. (2019). Dynamo action of the zonal winds in Jupiter. *Astronomy & Astrophysics*, *629*, A125. https://doi.org/10.1051/0004-6361/201935682

Wulff, P. N., Dietrich, W., Christensen, U. R., & Wicht, J. (2022). Zonal winds in the gas planets driven by convection above a stably stratified layer. *Monthly Notices of the Royal Astronomical Society*, *517*(4), 5584–5593. https://doi.org/10.1093/mnras/stac3045

Yadav, R. K., Cao, H., & Bloxham, J. (2022). A global simulation of the dynamo, zonal jets, and Vortices on Saturn. *The Astrophysical Journal*, *940*(2), 185. https://doi.org/10.3847/1538-4357/ac9d94

Yadav, R. K., Gastine, T., & Christensen, U. R. (2013). Scaling laws in spherical shell dynamos with free-slip boundaries. *Icarus*, *225*(1), 185–193. https://doi.org/10.1016/j.icarus.2013.02.030